



# Structural requirements of manganese oxides for methane oxidation: XAS spectroscopy and transition-state studies

Xiuyun Wang<sup>a</sup>, Yi Liu<sup>a</sup>, Yangyu Zhang<sup>a</sup>, Tianhua Zhang<sup>a</sup>, Huazhen Chang<sup>b</sup>, Yongfan Zhang<sup>a</sup>, Lilong Jiang<sup>a,\*</sup>

<sup>a</sup> National Engineering Research Center of Chemical Fertilizer Catalyst, Fuzhou University, Fuzhou, Fujian, 350002, China

<sup>b</sup> School of Environment and Natural Resources, Renmin University of China, Beijing 100872, China

## ARTICLE INFO

### Keywords:

Mn oxides  
Crystallographic structure  
Methane combustion  
H<sub>2</sub>O/CO<sub>2</sub>  
DFT + U calculation

## ABSTRACT

Different crystallographic structures of Mn oxides usually lead to diverse coordination geometries and oxidation states of MnO<sub>6</sub>, which in turn show strikingly different catalytic activities. In this study, methane oxidation performances over Mn oxides with various crystalline structures were investigated, including α-MnO<sub>2</sub> (double chains of Mn<sup>4+</sup>O<sub>6</sub> octahedra), α-Mn<sub>2</sub>O<sub>3</sub> (symmetry-inequivalent Mn<sup>3+</sup>O<sub>6</sub>), two-dimensional mesoporous β-MnO<sub>2</sub> (labels as Meso-MnO<sub>2</sub>, single chains of Mn<sup>4+</sup>O<sub>6</sub> octahedra) and one-dimensional β-MnO<sub>2</sub> (single chains of Mn<sup>3+/4+</sup>O<sub>6</sub> octahedra). The results demonstrate that the methane oxidation activities are dependent on their crystallographic structures, and follow an order of α-MnO<sub>2</sub> > β-MnO<sub>2</sub> > α-Mn<sub>2</sub>O<sub>3</sub> > Meso-MnO<sub>2</sub>. Meanwhile, α-MnO<sub>2</sub> exhibits good durability and excellent 9.5vol%H<sub>2</sub>O/10vol%CO<sub>2</sub> resistance ability. EXAFS, Raman, XPS, O<sub>2</sub>-TPD-MS and CH<sub>4</sub>-TPR-MS studies indicate that the outstanding catalytic activity over α-MnO<sub>2</sub> is due to higher surface Mn concentration, more active oxygen species and mono-μ-oxo bridged corner-shared [MnO<sub>6</sub>] sites, and excellent reducibility. More importantly, a new insight into reaction mechanism of methane oxidation over Mn oxides was proposed at the molecular level.

## 1. Introduction

Methane (CH<sub>4</sub>), as the main component of natural gas, has a greenhouse effect more than 20 times that of CO<sub>2</sub>. Combustion catalysts have been extensively explored to reduce the emission of CH<sub>4</sub>, and the catalytic combustion of CH<sub>4</sub> at relatively low temperature (< 600 °C) has been a topic of interest for decades [1]. Supported noble metal catalysts, especially palladium-based ones, are observed to have the best activities for CH<sub>4</sub> combustion, but high precious metal loading is needed, which restricts their further application because of high cost and sintering at high temperature [2].

A promising alternative to the precious-metal-based catalysts is the use of transition-metal oxides (TMOs) including MnO<sub>2</sub>, Co<sub>3</sub>O<sub>4</sub>, NiO, etc., among which Mn oxides is one of the most efficient catalysts in CH<sub>4</sub> oxidation [3]. However, the catalytic activity of the promising TMOs candidates is still not satisfactory at low temperature [4]. Recently, many studies have demonstrated that catalytic activities are dependent on catalyst compositions and crystallographic structures, shapes and pore structures, and there is a strong relationship between these properties and catalytic performance of a catalyst [5]. Therefore, the design and controllable preparation of Mn oxides catalyst is a key to

achieve a considerably high catalytic activity as that of noble metals. The different polymorphic structures of Mn oxides, such as α- and β-MnO<sub>x</sub>, display different ways to link together the basic octahedral [MnO<sub>6</sub>] units, thereby showing strikingly different catalytic activities [6]. Additionally, a general picture for the oxidation of methane over Mn oxides has not been established [7]. Contradictory claims on the oxidation of methane were reported such as that based on Langmuir-Hinshelwood (L-H) mechanism involving adsorbed oxygen and that based on Mars-van Krevelen (MvK) mechanism concerning lattice oxygen [8–10]. After all, it is believed that methane are activated by surface adsorbed oxygen species following the L-H route. Meanwhile, the L-H route may contend with an indirect oxidation process that involves lattice oxygen (MvK route) [8], depending on whether there is the formation of oxygen vacancies. Nonetheless, the MvK route has been proposed for the oxidation of C–H bond over TMOs with d<sup>0</sup> configuration [7], where the activation of O<sub>2</sub> via electron transfer is impossible over the empty d-bands. On the contrary, p-type TMOs such as those of Mn<sup>4+</sup> (d<sup>n > 0</sup>), can activate O<sub>2</sub> to generate surface active oxygen species via the L-H route through the donation of electrons. Therefore, it is necessary to elucidate the reaction pathways of methane oxidation over Mn oxides at a molecular level.

\* Corresponding author.

E-mail address: [jl@fzu.edu.cn](mailto:jl@fzu.edu.cn) (L. Jiang).

<https://doi.org/10.1016/j.apcatb.2018.02.007>

Received 6 October 2017; Received in revised form 31 January 2018; Accepted 3 February 2018

Available online 06 February 2018

0926-3373/ © 2018 Elsevier B.V. All rights reserved.

Herein, various structures of Mn oxides including  $\alpha$ -MnO<sub>2</sub> (double chains of Mn<sup>4+</sup>O<sub>6</sub> octahedra),  $\alpha$ -Mn<sub>2</sub>O<sub>3</sub> (double chains symmetry-in-equivalent Mn<sup>3+/4+</sup>O<sub>6</sub>), Meso-MnO<sub>2</sub> (single chains of Mn<sup>4+</sup>O<sub>6</sub> octahedra) and  $\beta$ -MnO<sub>2</sub> (single chains of Mn<sup>3+/4+</sup>O<sub>6</sub> octahedra) were synthesized by facile methods. The synthesized Mn oxides were systematically studied in the catalytic oxidation of CH<sub>4</sub>. A detailed investigation on the catalyst structures for the catalytic oxidation of methane over synthesized Mn oxides was conducted by means of Raman and XAS, reaction kinetics, XPS and *in situ* DRIFTS, aiming to acquire insights into the reaction mechanism at a molecular level. The results demonstrate that the catalytic activity for methane oxidation is closely associated with mono- $\mu$ -oxo bridged corner-shared MnO<sub>6</sub> sites, surface Mn concentration and oxygen species as well as reducibility.

## 2. Experimental

### 2.1. Catalyst preparation

The preparation of  $\alpha$ -MnO<sub>2</sub> nanowires consists of the following steps. 3 mol MnSO<sub>4</sub>·H<sub>2</sub>O and 2 mol KMnO<sub>4</sub> were dissolved into 50 mL distilled water. Then, the solution was moved to a Teflon-lined stainless-steel autoclave of 100 mL, and the sealed autoclave with its content was heated at 160 °C for 12 h. Thereafter, the obtained precipitate was washed with deionized water for several times, and successive drying at 100 °C. Ultimately, the powders were calcined at 500 °C for 3 h, and the obtained catalyst is labeled herein as  $\alpha$ -MnO<sub>2</sub>.

Highly ordered mesoporous Meso-MnO<sub>2</sub> was prepared via the nanocasting method. 1 g Mn(NO<sub>3</sub>)<sub>2</sub>·4H<sub>2</sub>O was dissolved in ethanol (60 mL). After stirring at 25 °C for 1 h, 0.5 g SBA-15 was added into the above solution. The suspension was stirred and followed by calcination at 500 °C for 3 h. Finally, the SBA-15 hard template was removed using 2 M NaOH solution at 60 °C under stirring conditions. Centrifugal separation was used to eliminate sodium silicate, and the sample was dried. The obtained catalyst is labeled as Meso-MnO<sub>2</sub>.

The synthetic procedure of  $\beta$ -MnO<sub>2</sub> nanorod was similar to that of  $\alpha$ -MnO<sub>2</sub> nanowires. 4 mol MnSO<sub>4</sub>·H<sub>2</sub>O and 5 mol (NH<sub>4</sub>)<sub>2</sub>S<sub>2</sub>O<sub>8</sub> were dissolved in 160 mL of distilled water to generate a homogeneous solution, which was then moved to a 100 mL Teflon-lined stainless steel autoclave, and the sealed autoclave with its content was heated at 140 °C for 12 h. The subsequent steps were identical to those described for the synthesis of the  $\alpha$ -MnO<sub>2</sub> nanowires.

$\alpha$ -Mn<sub>2</sub>O<sub>3</sub> was obtained by decomposition of MnCO<sub>3</sub> at 500 °C for 3 h under air.

### 2.2. Testing of catalytic activity

The catalytic performances were tested in a continuous flow fixed-bed quartz reactor (i.d. = 6.0 mm). Before activity test, 0.1 g of the sample (40–60 mesh) was treated with Ar at 350 °C for 30 min. The gas mixture composed of 1%CH<sub>4</sub>, 20% O<sub>2</sub> and balance N<sub>2</sub>. The total gas flow rate is 150 mL/min and corresponds to a weight hourly space velocity (WHSV) of 90,000 mL/(g h). After steady operation of 30 min, the inlet and outlet gases were tested by an on-line gas chromatograph (Agilent 7890A, USA) equipped with flame ionization detector (FID) and thermal conductivity detector (TCD). To examine the effects of CO<sub>2</sub> on methane conversion, we conduct the oxidation of methane in the presence of 10.0 vol% CO<sub>2</sub> in  $\alpha$ -MnO<sub>2</sub>. For water vapor addition, 9.5 vol % of H<sub>2</sub>O was provided by a mass flow controller using a water saturator. The methane conversion ( $X_{\text{methane}}$ ) and turnover frequency of TOF<sub>Mn</sub> were calculated according to the following equations:

$$X_{\text{methane}} = \frac{C_{\text{in}} - C_{\text{out}}}{C_{\text{out}}} \times 100\% \quad (1)$$

$$\text{TOF}_{\text{Mn}} = \frac{C_{\text{methane}} \times X_{\text{methane}} \times V_{\text{gas}}}{n_{\text{Mn}}} \quad [\text{s}^{-1}] \quad (2)$$

where  $C_{\text{in}}$  and  $C_{\text{out}}$  are the inlet and outlet methane concentration, respectively,  $V_{\text{gas}}$  represents the total molar flow rate,  $C_{\text{methane}}$  is the methane concentration in the inlet gas;  $n_{\text{Mn}}$  is the molar amounts of Mn. The kinetics parameter was measured while the oxidation of methane was conducted in the fixed-bed reactor, having the conversions kept below 19%.

### 2.3. Characterization

Powder X-ray diffraction (XRD) was measured on a Panalytical X'Pert Pro diffractometer using Co-K $\alpha$  radiation. N<sub>2</sub> physisorption measurements were carried out at 77 K on an ASAP 2020 apparatus. Scanning Electron Microscope (SEM) was performed on a JSM6700-F instrument. High-resolution transmission electron microscopy (HR-TEM) measurement was measured on a JEM-2010 microscope. H<sub>2</sub> temperature-programmed reduction (H<sub>2</sub>-TPR) was measured on an AutoChem II 2920 equipment using TCD, having the catalyst treated in an Ar flow (30 mL/min) at 400 °C for 30 min. After cooling to room temperature, the sample was heated to 700 °C in a gas flow of H<sub>2</sub>/Ar (vol/vol = 10/90; rate = 30 mL/min). O<sub>2</sub>-TPD-MS and CH<sub>4</sub>-TPR-MS experiments were carried out on a Micromeritics Autochem II 2920 instrument equipped with a Hiden QIC-20 mass spectrometer (for more details see the supporting information).

X-ray photoelectron spectroscopy (XPS) analysis was tested on Physical Electronics Quantum 2000, equipped with monochromatic Al-K $\alpha$  source ( $K_{\alpha}$  = 1486.6 eV) and a charge neutralizer. Raman spectra of samples were collected under ambient condition on a Renishaw spectrometer, and a laser beam ( $\lambda$  = 532 nm) was used for excitation. X-ray absorption near edge structure (XANES) and the extended X-ray absorption fine structure (EXAFS) measurements were undertaken at Beamlines 1W1B at Beijing Synchrotron Radiation Facility (BSRF). *In situ* diffuse reflection infrared Fourier transform spectroscopy (DRIFTS) was performed on a Nicolet Nexus FT-IR spectrometer in the range of 650–4000 cm<sup>−1</sup> (for more details see the supporting information). DFT + U calculations with dispersion corrections were performed utilizing the VASP and PAW method (for more details see the supporting information).

## 3. Results and discussions

### 3.1. Morphologic, structural and textural characterization

X-ray diffraction peaks (Fig. 1) in  $\alpha$ -MnO<sub>2</sub> are assigned to the tetragonal MnO<sub>2</sub>, with lattice constants  $a$  = 9.8150 Å and  $c$  = 2.8470 Å. The crystalline nature of  $\alpha$ -MnO<sub>2</sub> is also evidenced by the TEM images, which show a uniform nanowire morphology (Fig. 2A) with diameter about 28 nm (Fig. 2B). The interplanar distances of 0.473 and 0.278 nm

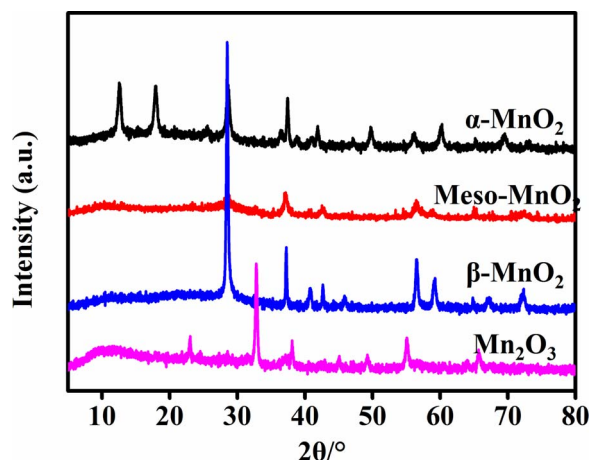


Fig. 1. XRD patterns of  $\alpha$ -MnO<sub>2</sub>, Meso-MnO<sub>2</sub>,  $\beta$ -MnO<sub>2</sub> and  $\alpha$ -Mn<sub>2</sub>O<sub>3</sub>.

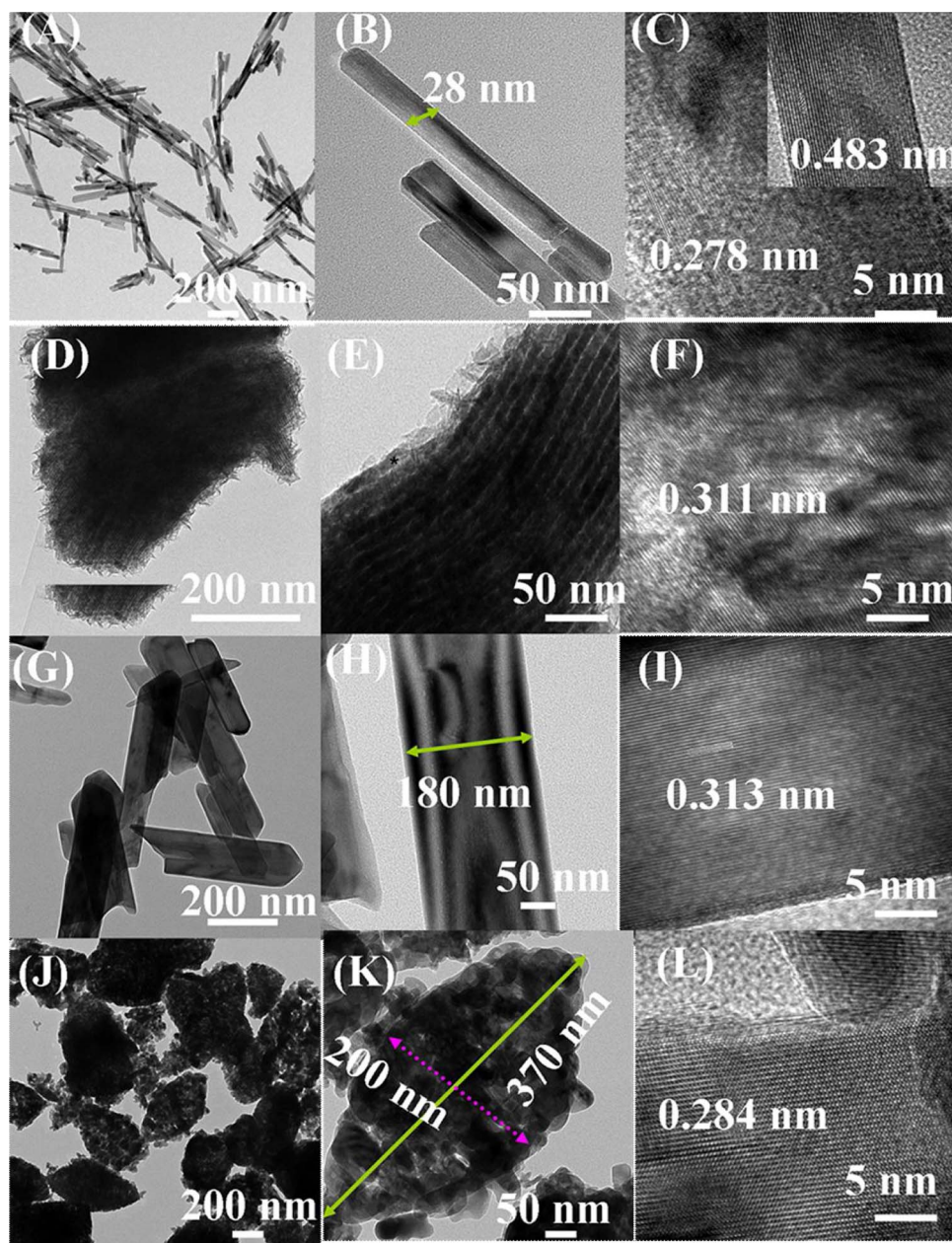


Fig. 2. TEM and HR-TEM images of (A–C)  $\alpha$ - $\text{MnO}_2$ ; (D–F) Meso- $\text{MnO}_2$ ; (G–I)  $\beta$ - $\text{MnO}_2$  and (J–L)  $\alpha$ - $\text{Mn}_2\text{O}_3$ .

correspond to (100) and (101) planes of  $\alpha$ - $\text{MnO}_2$  (Fig. 2C). The statistical results of HR-TEM images (Fig. S1) show that the mainly exposed crystal facet of  $\alpha$ - $\text{MnO}_2$  is (100). The XRD pattern of Meso- $\text{MnO}_2$  shows several weak diffraction peaks correspond to  $\beta$ - $\text{MnO}_2$  phase. To be noted, TEM (Fig. 2D–F) and HR-TEM (Fig. 2E) images illustrate that Meso- $\text{MnO}_2$  shows highly ordered nature of mesoporous framework. Moreover, the low-angle XRD pattern (Fig. S2) of Meso- $\text{MnO}_2$  presents three diffraction peaks, which can be assigned to (10), (11) and (20) reflections, matching with the p6m symmetry characteristic for the two-dimensional order mesoporous structure. XRD peaks of  $\beta$ - $\text{MnO}_2$  correspond to the standard diffraction characteristic of pyrolusite. TEM images (Fig. 2G–I) show that  $\beta$ - $\text{MnO}_2$  exhibits a nanorod morphology with a  $2\mu\text{m}$  (L)  $\times$  180 nm (i.d.) dimension. HR-TEM image (Fig. 2I) shows that  $\beta$ - $\text{MnO}_2$  displays an interplanar distance of 0.313 nm, which is associated with  $\text{MnO}_2$  (110) facet. It reveals that the nanorod has a preferential growth along the [001] direction, which is perpendicular to the [110] direction. In the  $\text{Mn}(\text{CO}_3)_2$  pyrolysis derived flower-like (Fig. S2D and Fig. 2L) manganese oxide with a cubic  $\alpha$ - $\text{Mn}_2\text{O}_3$  phase. The

relatively small  $d$  spacing is confirmed by HR-TEM in Fig. 2O; i.e., an interplanar distance of 0.284 nm matches with the (111) planar spacing.

$\alpha$ - $\text{MnO}_2$  structure is constructed by double chains of  $[\text{MnO}_6]$  octahedra (Fig. 3A), while  $\beta$ - $\text{MnO}_2$  is comprised of single chains of edge-sharing  $[\text{MnO}_6]$  octahedra (Fig. 3B) [11]. However,  $\text{Mn}_2\text{O}_3$  has a close-packed structure and has five symmetry-inequivalent  $\text{Mn}^{3+}\text{O}_6$  sites in the unit cell (Fig. 3D) [11]. The textural properties of as-prepared samples were characterized by  $\text{N}_2$  adsorption (Fig. S3 and Table 1). Meso- $\text{MnO}_2$  displays the highest BET surface area ( $110\text{ m}^2/\text{g}$ ) and the largest pore volume ( $0.508\text{ cm}^3/\text{g}$ ), while  $\beta$ - $\text{MnO}_2$  possesses the lowest surface area ( $12\text{ m}^2/\text{g}$ ) and the smallest pore volume ( $0.08\text{ cm}^3/\text{g}$ ). In the case of  $\alpha$ - $\text{MnO}_2$  and  $\alpha$ - $\text{Mn}_2\text{O}_3$ , they show BET surface area of 24 and  $29\text{ m}^2/\text{g}$ , respectively.



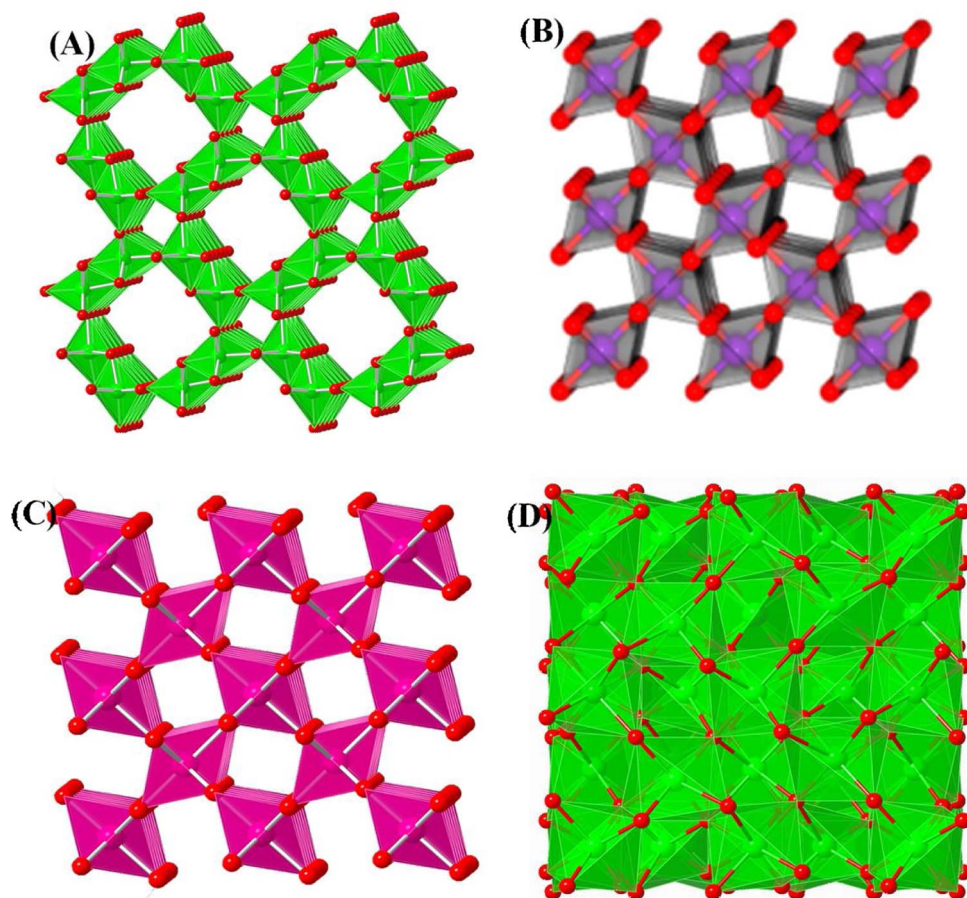


Fig. 3. Structural depictions of (A)  $\alpha$ -MnO<sub>2</sub>; (B) Meso-MnO<sub>2</sub>; (C)  $\beta$ -MnO<sub>2</sub> and (D)  $\alpha$ -Mn<sub>2</sub>O<sub>3</sub>.

### 3.2. Catalytic performances

#### 3.2.1. Catalytic activity and kinetic studies

The catalytic performances of methane oxidation over Mn oxides are shown in Fig. 4A. The temperatures at a methane conversion of 50% ( $T_{50}$ ) and 90% ( $T_{90}$ ), are both important indicators of catalytic combustion activity, which are listed in Table 1. The results suggest that catalytic efficiency is in the order of  $\alpha$ -MnO<sub>2</sub> >  $\beta$ -MnO<sub>2</sub> >  $\alpha$ -Mn<sub>2</sub>O<sub>3</sub> > Meso-MnO<sub>2</sub> at 200–425 °C. Specifically, the  $T_{50\%}$  and  $T_{90\%}$  values of  $\alpha$ -MnO<sub>2</sub> are 355 and 415 °C, respectively, which are much lower than those of  $\beta$ -MnO<sub>2</sub> and  $\alpha$ -Mn<sub>2</sub>O<sub>3</sub>. Notably, methane conversion in  $\beta$ -MnO<sub>2</sub> is higher than that in  $\alpha$ -Mn<sub>2</sub>O<sub>3</sub> at 200–425 °C, but lower at 425–500 °C. Moreover, the turnover frequency per surface Mn (TOF<sub>Mn</sub>) values (Fig. 4B) obey the order of  $\alpha$ -MnO<sub>2</sub> >  $\beta$ -MnO<sub>2</sub> >  $\alpha$ -Mn<sub>2</sub>O<sub>3</sub> > Meso-MnO<sub>2</sub>. The result further confirms that  $\alpha$ -MnO<sub>2</sub> exhibits the highest catalytic efficiency. Additionally,  $\alpha$ -MnO<sub>2</sub> exhibits good durability in methane combustion (Fig. 4C), attaining CO<sub>2</sub> selectivity more than 98% in the whole period.

The kinetic studies of methane combustion over the catalysts were performed with methane conversion kept less than 20%. Based on the

slopes of the Arrhenius plots (Fig. 4D), the apparent activation energies (Table 1) decrease in the order of Meso-MnO<sub>2</sub> (93 kJ/mol) >  $\alpha$ -Mn<sub>2</sub>O<sub>3</sub> (64 kJ/mol) >  $\beta$ -MnO<sub>2</sub> (61 kJ/mol) >  $\alpha$ -MnO<sub>2</sub> (55 kJ/mol), matching with the sequence of catalytic performance at 200–425 °C. The  $E_a$  in  $\alpha$ -MnO<sub>2</sub> is found to be lower than those of some Pt-based catalysts (67–138 kJ mol<sup>−1</sup>). These results indicate that relatively lower reaction temperature and higher TOF<sub>Mn</sub> value among the as-prepared catalysts makes the  $\alpha$ -MnO<sub>2</sub> a promising catalyst for methane combustion. To investigate the structure-efficiency relationship, more characterization is needed.

#### 3.2.2. Effects of H<sub>2</sub>O and CO<sub>2</sub>

To examine the effects of H<sub>2</sub>O and CO<sub>2</sub> on methane conversion, we conduct the catalytic oxidation of methane in the presence of 9.5 vol% H<sub>2</sub>O and/or 10.0 vol% CO<sub>2</sub> in  $\alpha$ -MnO<sub>2</sub>. As shown in Fig. 5A, the addition of 9.5 vol% H<sub>2</sub>O results in an obvious decrement of methane conversion at relatively low-temperature ( $T < 350$  °C). These results indicate that the competitive adsorption of H<sub>2</sub>O and CH<sub>4</sub>/O<sub>2</sub> on MnO<sub>2</sub>, and the adsorption of H<sub>2</sub>O is stronger than that of CH<sub>4</sub>/O<sub>2</sub> [12a], which has been proved by *in situ* DRIFT spectroscopy (*infra*). Notably, the

Table 1

Textural properties, surface element concentration, reaction temperature,  $O_{\text{latt}}/(O_{\text{ads}} + O_{\text{latt}})$  ratio and activation energy ( $E_a$ ) of catalysts.

Sample	$S_{\text{BET}}$ (m <sup>2</sup> g <sup>−1</sup> )	Pore volume (cm <sup>3</sup> g <sup>−1</sup> )	Average pore radius (nm)	Surface Mn Concentration <sup>a</sup> (%)	$T_{50\%}$ (°C)	$T_{90\%}$ (°C)	$O_{\text{latt}}/(O_{\text{ads}} + O_{\text{latt}})$ (%)	$E_a$ (kJ/mol)
$\alpha$ -MnO <sub>2</sub>	24	0.148	12.4	27.6	355	415	67	55
Meso-MnO <sub>2</sub>	110	0.508	9.2	20.1	456	–	44	93
$\beta$ -MnO <sub>2</sub>	12	0.080	16.8	22.3	388	499	63	61
$\alpha$ -Mn <sub>2</sub> O <sub>3</sub>	29	0.187	12.8	26.6	408	481	67	64

<sup>a</sup> XPS results.

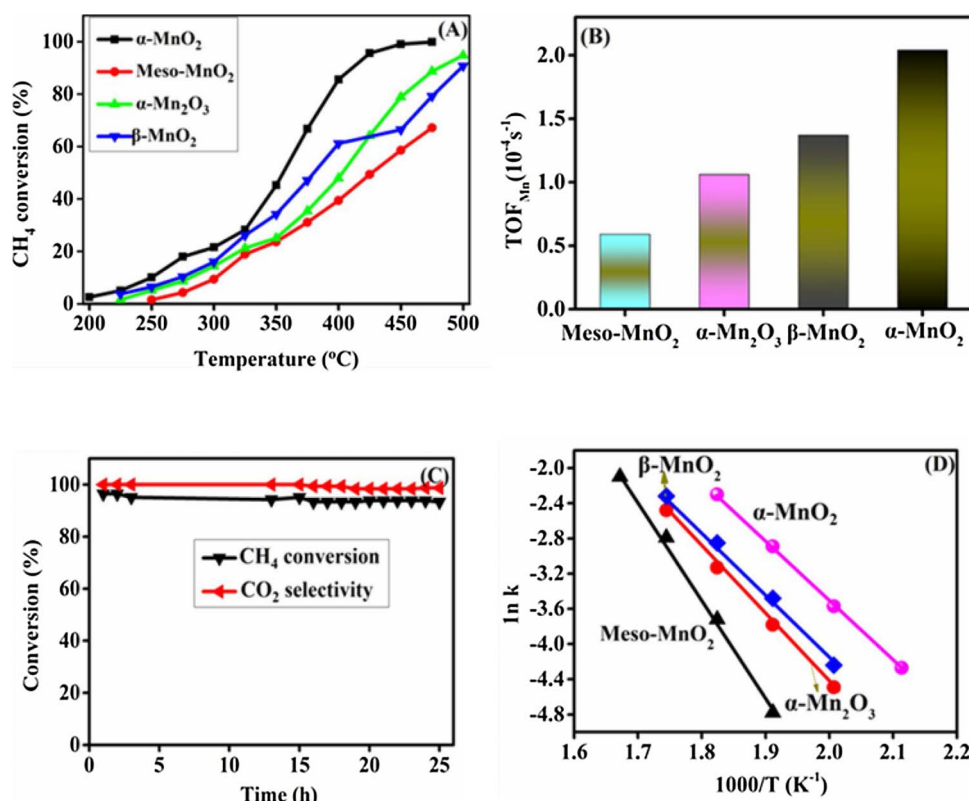


Fig. 4. (A) Methane conversion as a function of temperature; (B) TOF<sub>Mn</sub> of as-prepared catalysts at 275 °C; (C) time on stream of methane conversion and CO<sub>2</sub> selectivity over α-MnO<sub>2</sub> at 500 °C. (D) Arrhenius plots for methane oxidation.

addition of 9.5 vol% H<sub>2</sub>O has little effect on methane conversion with only a slight deactivation by less than 3% at a relative high temperature ( $T > 350$  °C), which may be associated with strong lattice oxygen mobility at high temperature, leading to the adsorption of oxygen is stronger than that of H<sub>2</sub>O [12a]. However, the addition of 10 vol% CO<sub>2</sub> results in an obvious decrement of methane conversion, which can be ascribed to surface active sites of α-MnO<sub>2</sub> are covered by carbonate species [12]. The significant effect of CO<sub>2</sub> on the methane conversion over α-MnO<sub>2</sub> demonstrate in the present study agrees well with the previous reports [12].

Additionally, the stability of α-MnO<sub>2</sub> was also tested by a time-on-stream experiment where the catalyst was kept on-line at 475 °C in the presence of 9.5 vol% H<sub>2</sub>O and/or 10.0 vol% CO<sub>2</sub>. Fig. 5B indicates that no significant change in catalytic activity is found in α-MnO<sub>2</sub> in the presence of 9.5 vol% H<sub>2</sub>O. The addition of 10 vol% CO<sub>2</sub> results in a decrement of methane conversion from 99% to 93% in α-MnO<sub>2</sub>. Notably, the co-existence of 9.5 vol% H<sub>2</sub>O and 10 vol% CO<sub>2</sub> lead to a

decrement of methane conversion from 99% to 93% in α-MnO<sub>2</sub>. These results indicate that the significant effect of CO<sub>2</sub> on the methane conversion over α-MnO<sub>2</sub> at low temperature rather than high temperature. In order to understand the effect of CO<sub>2</sub> on the catalytic stability over α-MnO<sub>2</sub> at different temperatures, XPS of used α-MnO<sub>2</sub> have been added in Fig. S4. XPS spectrum of Mn 2p shows that surface Mn concentration is decreased from 27.6% in fresh MnO<sub>2</sub> to 16.29% in the used counterpart (10% CO<sub>2</sub>, 1% CH<sub>4</sub>, 20% O<sub>2</sub> and balance N<sub>2</sub> at 350 °C for 5 h) (Table S1), indicating that partial surface Mn active sites are covered by carbonate species [12], therefore an obvious decrease in catalytic stability. Interestingly, surface Mn concentration over used α-MnO<sub>2</sub>-475 °C (10% CO<sub>2</sub>, 1% CH<sub>4</sub>, 20% O<sub>2</sub> and balance N<sub>2</sub> at 475 °C for 5 h) is slightly decreased to 25.21% (Table S1), probably due to that surface carbonate species are decomposed at such a high temperature.

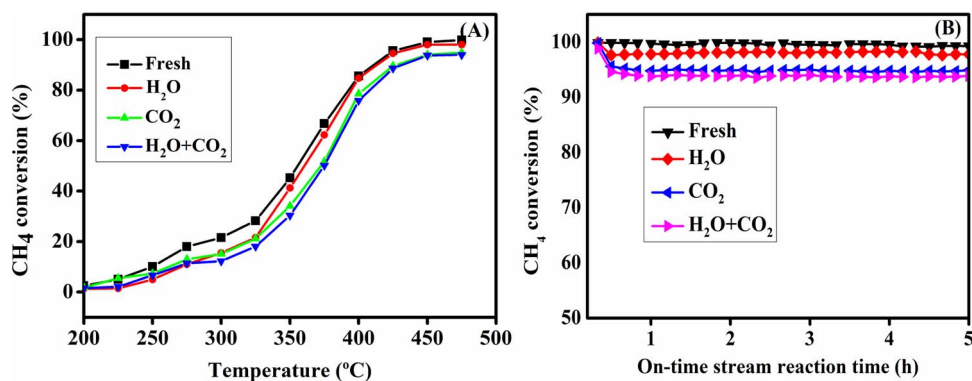


Fig. 5. (A) Effect of 9.5 vol% H<sub>2</sub>O and 10 vol% CO<sub>2</sub> on methane conversion at different reaction temperatures in α-MnO<sub>2</sub>. (B) Effect of 9.5 vol% H<sub>2</sub>O and 10 vol% CO<sub>2</sub> on methane conversion at 475 °C in α-MnO<sub>2</sub>.

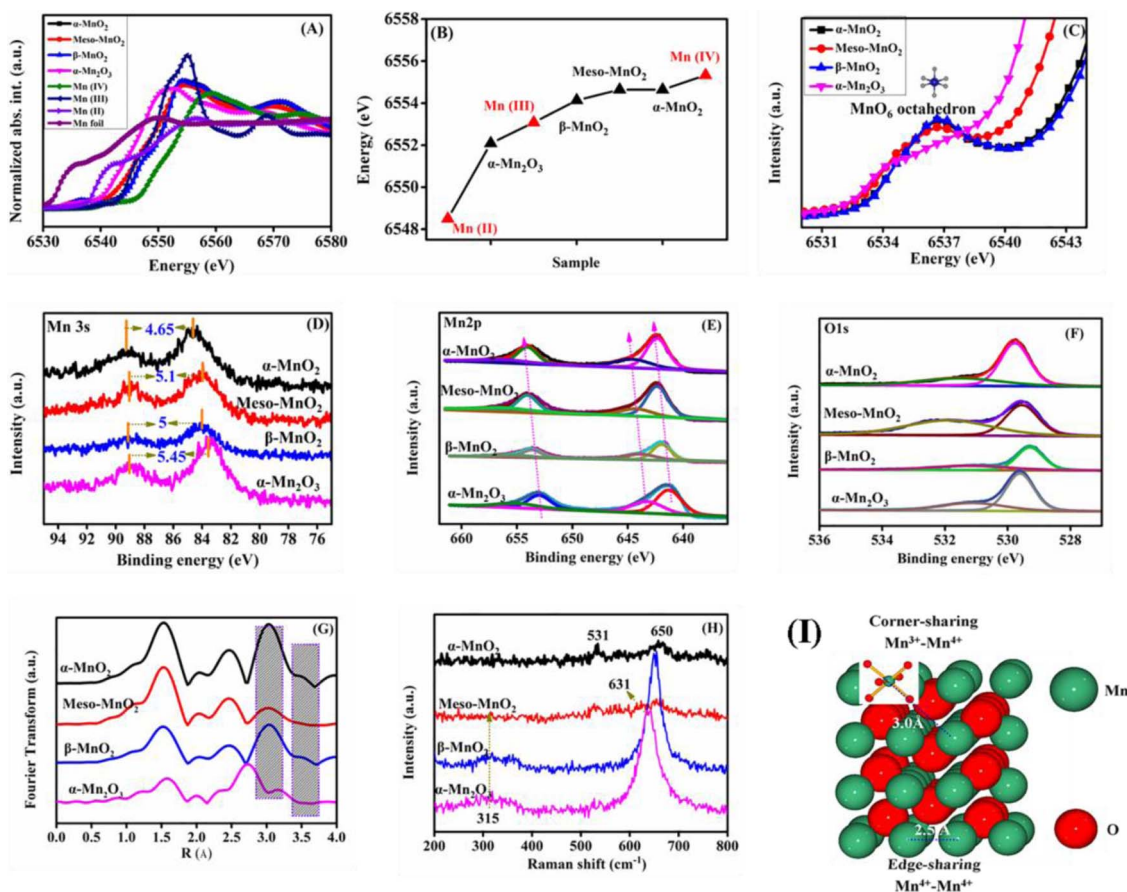


Fig. 6. (A) Normalized Mn K-edge XANES spectra; (B) The energy position of main absorption of Mn K-edge; (C) Pre-edge of XANES spectra at the Mn K-edge of catalysts; (D) XPS Mn3s spectra; (E) Mn2p, (F) O1s, (G) Mn K-edge EXAFS spectra, (H) Raman spectra and the relation of interatomic distance in (I) MnO<sub>2</sub> structure.

### 3.3. Oxidation states and electronic structure

X-ray absorption near-edge spectroscopy (XANES) was employed to clarify the oxidation states of Mn species, and the results are shown in Fig. 6A–C. The Mn valence states (Fig. 6A–B) of the catalysts follow the order of:  $\alpha$ -MnO<sub>2</sub> (+3.78)  $\sim$  Meso-MnO<sub>2</sub> (+3.77)  $>$   $\beta$ -MnO<sub>2</sub> (+3.53)  $>$   $\alpha$ -Mn<sub>2</sub>O<sub>3</sub> (+2.79). These results indicate that the dominant state of Mn ions in  $\alpha$ -MnO<sub>2</sub> and  $\alpha$ -Mn<sub>2</sub>O<sub>3</sub> are +4 and +3, respectively. However, the co-existence of Mn<sup>3+</sup> (47%) and Mn<sup>4+</sup> (53%) ions in  $\beta$ -MnO<sub>2</sub>. Additionally,  $\alpha$ -MnO<sub>2</sub>, Meso-MnO<sub>2</sub> and  $\beta$ -MnO<sub>2</sub> (Fig. 6C) exhibit a broad pre-edge peak, indicating the stabilization of Mn ions over the octahedral site because of the separation of degenerated 3d levels under the octahedral crystal field of 1s  $\rightarrow$  3d ( $t_{2g}$ ) and 1s  $\rightarrow$  3d ( $e_g$ ) transition [13].

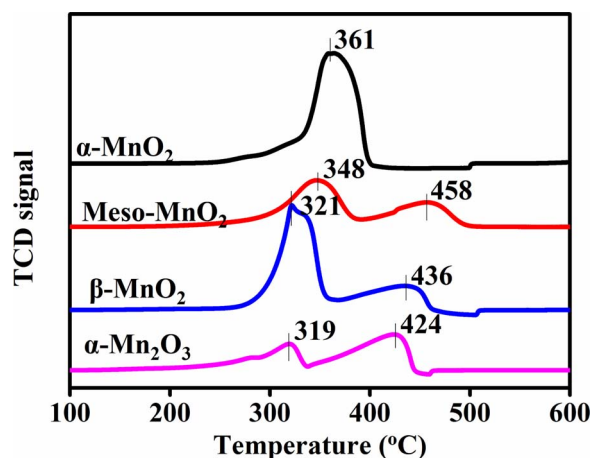
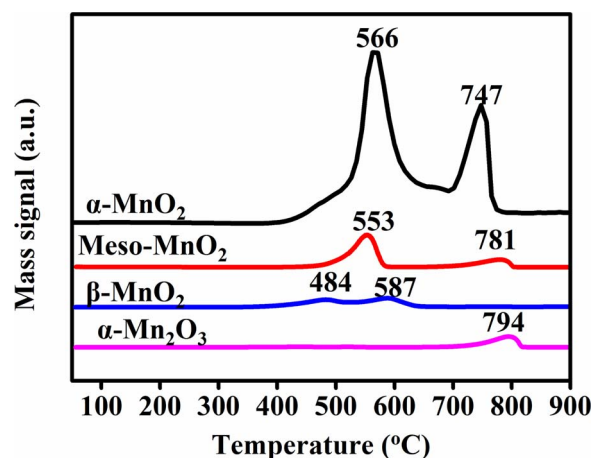
The surface oxidation state of Mn was further investigated by XPS. Notably,  $\Delta$ Mn3s in MnO<sub>x</sub> is in the order of  $\alpha$ -MnO<sub>2</sub> (4.65)  $<$   $\beta$ -MnO<sub>2</sub> (5.0)  $<$  Meso-MnO<sub>2</sub> (5.10)  $<$   $\alpha$ -Mn<sub>2</sub>O<sub>3</sub> (5.45). The larger value of Mn3s peak splitting, the more Mn<sup>3+</sup> species on the surface [13]. That is,  $\alpha$ -Mn<sub>2</sub>O<sub>3</sub> possesses the largest amount of surface Mn<sup>3+</sup> species. The binding energies of Mn2p<sub>3/2</sub> for  $\alpha$ -MnO<sub>2</sub> are more than 642 eV, indicating surface Mn valence state is close to +4. This is supported by the magnitude of  $\Delta$ E3s, which are in the range between 4.4 eV (+4) and 5.1 eV (+3) [14]. Additionally, XPS spectra of Mn2p<sub>3/2</sub> results (Fig. 6E) further indicate that the co-existence of Mn<sup>3+</sup> (642.0 eV) and Mn<sup>4+</sup> (644.0 eV) in  $\beta$ -MnO<sub>2</sub> [15].

Meanwhile, structural defects can be correlated with the O1s spectra shown in Fig. 6F. The peak at 529.3–529.8 eV can be assigned to lattice oxygen (O<sub>latt</sub>), while that at 531.1–531.4 eV to surface oxygen species (O<sub>ads</sub>), resulting from the adsorption of gaseous O<sub>2</sub> into oxygen vacancies [3]. The results demonstrate that the O<sub>latt</sub>/(O<sub>latt</sub> + O<sub>ads</sub>) ratio of

as-prepared catalysts follows the trend of Meso-MnO<sub>2</sub> (44%)  $<$   $\beta$ -MnO<sub>2</sub> (63%)  $<$   $\alpha$ -MnO<sub>2</sub> (67%)  $\sim$   $\alpha$ -Mn<sub>2</sub>O<sub>3</sub> (67%), suggesting that  $\alpha$ -MnO<sub>2</sub> and  $\alpha$ -Mn<sub>2</sub>O<sub>3</sub> display more surface oxygen vacancies [5]. After CH<sub>4</sub>-TPR test (vide infra), the surface atomic ratio of O/Mn in  $\alpha$ -MnO<sub>2</sub> is decrease to 0.52 in comparison with the fresh one (1.96), indicating that surface oxygen is obviously consumed during the reaction.

Moreover, Mn K-edge EXAFS spectra (Fig. 6G) of  $\alpha$ -MnO<sub>2</sub>, Meso-MnO<sub>2</sub> and  $\beta$ -MnO<sub>2</sub> and  $\beta$ -MnO<sub>2</sub> show several main ( $<$  4 Å) Fourier-transformed (FT) peaks at 1.53, 2.50 and 3.03 Å, corresponding to “Mn–O” shell, edge-shared and corner-shared “Mn–Mn” shells [15], respectively. The FT peak at 2.50 Å is associated with di- $\mu$ -oxo bridging (edge-shared) between Mn<sup>4+</sup> ions, while the FT peaks at 3.03 and 3.52 Å indicate the presence of mono- $\mu$ -oxo bridged Mn ions (corner-sharing octahedra) [16]. Base on the peak intensities, there are more mono- $\mu$ -oxo bridged (corner-shared) MnO<sub>6</sub> octahedra in  $\alpha$ -MnO<sub>2</sub> when compared to the other catalysts. Thus, a higher fraction of longer Mn–O–Mn bridges is existed in  $\alpha$ -MnO<sub>2</sub>, indicative of a more disordered structure. To be mentioned, the FT peaks values in  $\alpha$ -Mn<sub>2</sub>O<sub>3</sub> are slightly higher than that of the Mn<sub>2</sub>O<sub>3</sub> standard (Fig. S5), likely due to a mixture of MnO<sub>x</sub> phases. Raman spectra of fresh (Fig. 6H, for more details see the supporting information) and aged  $\alpha$ -MnO<sub>2</sub> (Fig. S6) further confirm that mono- $\mu$ -oxo bridged MnO<sub>6</sub> are involved in the catalytic reaction (for more details see the supporting information). In order to understand more clearly how is the interatomic distance related to the coordination geometry of different Mn ions, the schematics of interatomic distance of edge-shared and corner-shared “Mn–Mn” atoms in MnO<sub>2</sub> is presented in Fig. 6I. Combining with EXAFS, XPS and catalytic activity results, it can be inferred that mono- $\mu$ -oxo bridged MnO<sub>6</sub> sites and surface Mn concentration (Table 1) can be associated with the catalytic oxidation of methane.



Fig. 7.  $H_2$ -TPR profiles of as-prepared catalysts.Fig. 9.  $O_2$ -TPD-MS profiles of as-prepared catalysts.

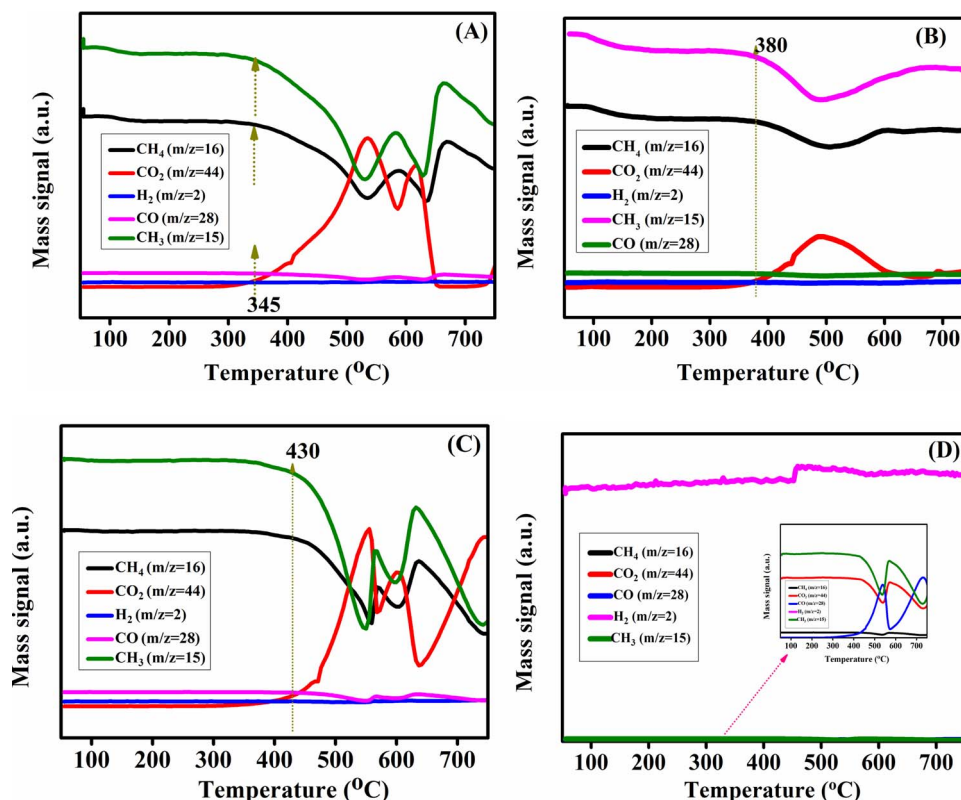
### 3.4. Reducibility and oxygen desorption properties

#### 3.4.1. $H_2$ -TPR and $CH_4$ -TPR

Reducibility performances of various samples were evaluated by  $H_2$ -TPR, and the results are illustrated in Fig. 7. As for  $MnO_2$ , the reduction process could be reasonably divided into two stages: (1)  $Mn^{4+}$  to  $Mn^{3+}$  and (2)  $Mn^{3+}$  to  $Mn^{2+}$  [5]. The reduction temperatures of Mn species in  $\beta$ - $MnO_2$  (321 and 436 °C) are lower than those of Meso- $MnO_2$  (348 and 458 °C) and  $\alpha$ - $MnO_2$  (361 °C), suggesting the former catalyst exhibits better low-temperature reducibility performance. Furthermore, the amount of  $H_2$  consumption (Table S2) is smaller than the theoretical amount (11.5 mmol/g) required for full reduction of  $MnO_2$  to  $MnO$ . The result implies the existence of Mn species of lower valence ( $< +4$ ), which is in consistent with the  $Mn2p_{2/3}$  XPS and Mn K-edge XANES results. Moreover,  $H_2$  consumption of 6.33 mmol/g is required if the  $Mn_2O_3$  is completely reduced to  $MnO$ . Herein, the total  $H_2$  consumption

is 5.66 mmol/g of the  $Mn_2O_3$ , indicating the existence of mixture Mn species.

To illustrate the reduction behaviors of as-prepared catalysts under a flowing methane environment, the profiles of  $CH_4$ -TPR-MS are presented in Fig. 8. For  $\alpha$ - $MnO_2$  (Fig. 8A), the first methane consumption peak is assigned to the reaction between  $CH_4$  and  $Mn^{4+}$  species starting from 345 °C. Meanwhile, the mass signal of  $CO_2$  and  $CH_3^*$  are observed at the same temperature, indicating that methane is activated and dehydrogenized to form  $CH_3^*$  and  $H_2$ . Then,  $CO_2$  is produced by the reaction of carbon intermediates with the lattice oxygen from  $MnO_2$ . The second methane consumption peak around 600–750 °C is accompanied by the formation of  $CH_3^*$  and  $CO$ , which could be due to the partial oxidation of methane by the oxygen species at the interface of Mn species ( $CH_4 + 2O_{interface} \rightarrow CO + 2H_2O$ ,  $CH_4 + O_{interface} \rightarrow CO + 2H_2$ ) and the  $CH_4$  cracking ( $2CH_4 \rightarrow 2CH_3 + H_2$ ) [17]. The reaction behavior in  $\beta$ - $MnO_2$  is similar to that in  $\alpha$ - $MnO_2$ . However, the

Fig. 8.  $CH_4$ -TPR-MS profiles of (A)  $\alpha$ - $MnO_2$ ; (B) Meso- $MnO_2$ ; (C)  $\beta$ - $MnO_2$  and (D)  $\alpha$ - $Mn_2O_3$ .

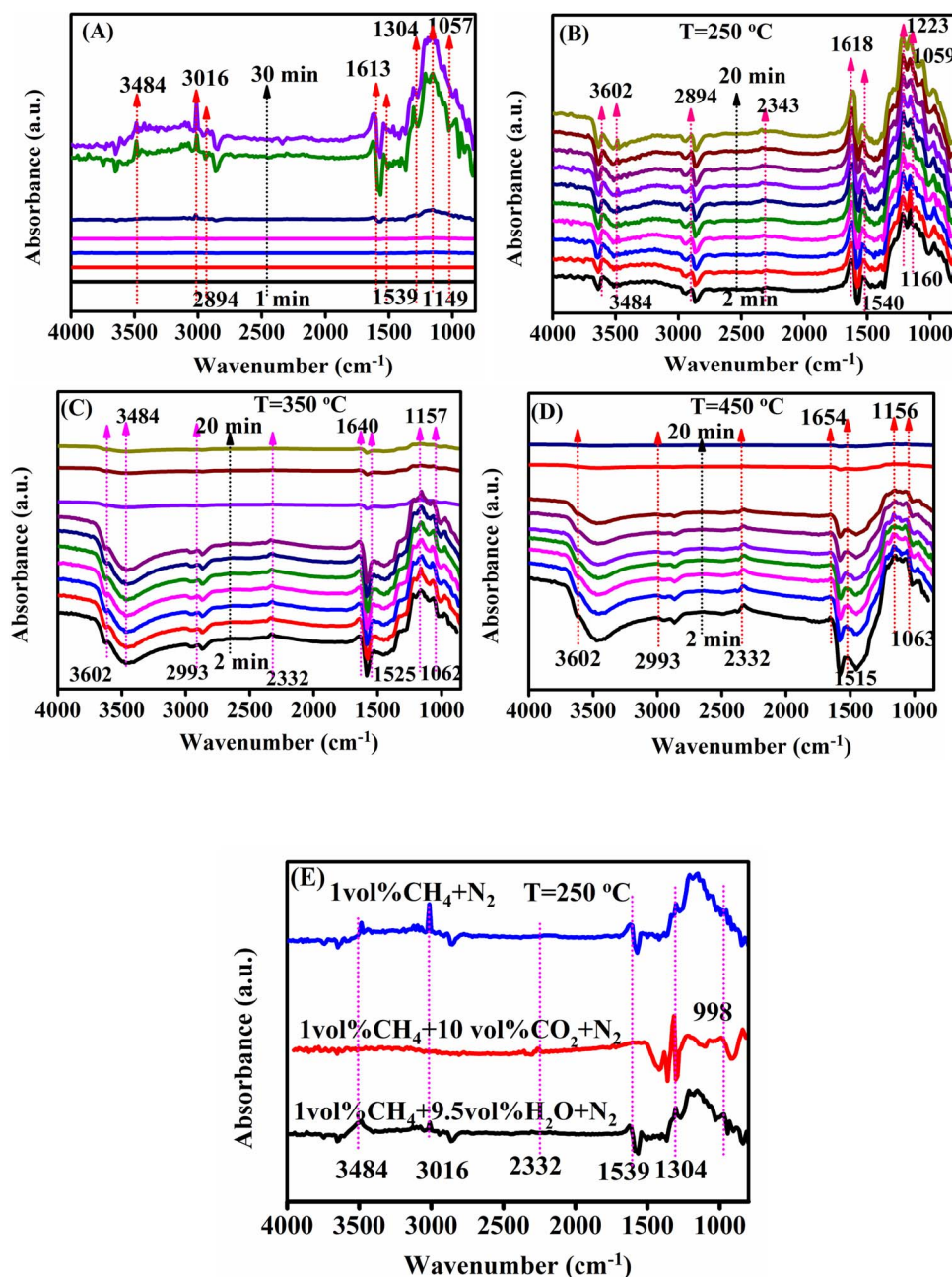


Fig. 10. (A) CH<sub>4</sub> adsorption at 250 °C in α-MnO<sub>2</sub>; (B) O<sub>2</sub> reacting with CH<sub>4</sub> pre-adsorbed at 250 °C in α-MnO<sub>2</sub>; (C) O<sub>2</sub> reacting with CH<sub>4</sub> pre-adsorbed at 350 °C in α-MnO<sub>2</sub>; (D) O<sub>2</sub> reacting with CH<sub>4</sub> pre-adsorbed at 450 °C in α-MnO<sub>2</sub> and (E) CH<sub>4</sub> adsorption at 250 °C in the presence of H<sub>2</sub>O and CO<sub>2</sub> over α-MnO<sub>2</sub>.

temperature of the methane consumption peaks for β-MnO<sub>2</sub> ( $T = 430$  °C, Fig. 8C) are much higher than that for α-MnO<sub>2</sub>, suggesting that α-MnO<sub>2</sub> possesses better methane combustion performance. Additionally, CH<sub>4</sub>-TPD-MS profiles of used α-MnO<sub>2</sub> are shown in Fig. S7. In the case of used MnO<sub>2</sub>-350 °C (Fig. S7A), the signals of CH<sub>3</sub><sup>+</sup>, CH<sub>4</sub> and CO<sub>2</sub> are different from those of fresh sample. The temperature of methane consumption peak is increased up to 383 °C, resulting in decreased methane conversion. In contrast, for used MnO<sub>2</sub>-475 °C, the signals of CH<sub>3</sub><sup>+</sup>, CH<sub>4</sub> and CO<sub>2</sub> are similar to those of fresh sample (Fig. S7B).

Notably, the second methane consumption peak is not observed in the case of Meso-MnO<sub>2</sub> (Fig. 8B). For α-Mn<sub>2</sub>O<sub>3</sub>, nevertheless, there are different reaction behaviors with varying temperature ranges (Fig. 8D). A higher concentration of CO and H<sub>2</sub> in α-Mn<sub>2</sub>O<sub>3</sub> indicates that Mn<sup>3+</sup> species can accelerate the lattice oxygen diffusion from the bulk to the interface to react with adsorbed CH<sub>3</sub> intermediates [18]. To be noted,

the temperature of the methane consumption peak for Meso-MnO<sub>2</sub> ( $T = 380$  °C) is lower than that of β-MnO<sub>2</sub> ( $T = 430$  °C), but the latter one exhibits better catalytic activity. The results suggest that there are other factors influencing the catalytic activity, such as Mn coordination environments and oxygen species.

#### 3.4.2. O<sub>2</sub>-TPD-MS

Notably, oxygen species in the redox reactions are usually transformed through the following pathway: O<sub>2</sub> (ad) → O<sub>2</sub><sup>-</sup> (ad) → O<sup>-</sup> (ad) → O<sup>2-</sup> (latt) [19]. Thus, O<sub>2</sub>-TPD-MS experiments of as-prepared catalysts were carried out. As shown in Fig. 9, oxygen desorbed at 400–600 °C and 600–800 °C are ascribed to superoxide peroxide (O<sup>-</sup>) and lattice oxygen (O<sup>2-</sup>), respectively [19]. Oxygen desorption peaks are observed in the cases of α-MnO<sub>2</sub> (566 and 747 °C), Meso-MnO<sub>2</sub> (553 and 781 °C) and β-MnO<sub>2</sub> (484 and 587 °C). The peak area (< 600 °C) in α-MnO<sub>2</sub> is much higher than other catalysts, indicating that α-MnO<sub>2</sub>



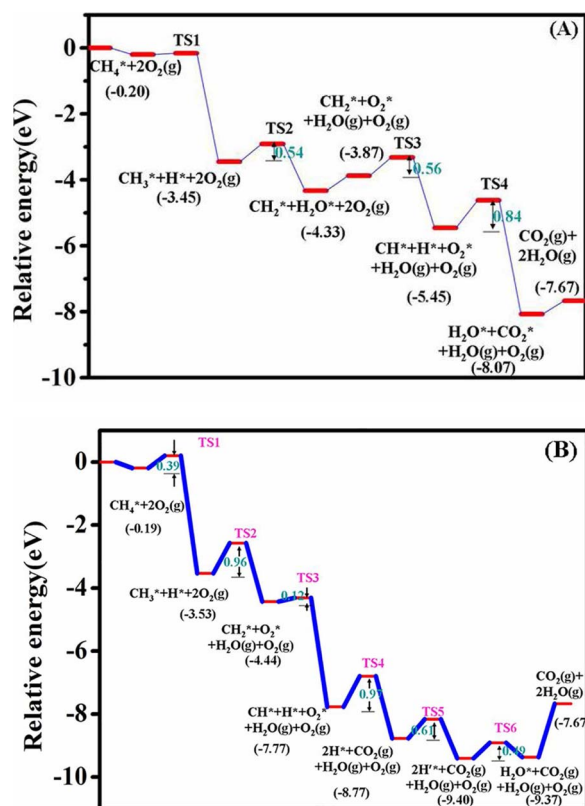


Fig. 11. The calculated energy profiles over (A)  $\alpha$ -MnO<sub>2</sub> (100) and (B)  $\beta$ -MnO<sub>2</sub> (101).

possesses more active oxygen species. Meanwhile, the desorption temperature of O<sup>2-</sup> (latt) in  $\alpha$ -MnO<sub>2</sub> (747 °C) is lower than those in Meso-MnO<sub>2</sub> (781 °C) and  $\alpha$ -Mn<sub>2</sub>O<sub>3</sub> (794 °C), implying that O<sup>2-</sup> (latt) is released in an easier manner for  $\alpha$ -MnO<sub>2</sub> [17]. The relatively easy release of O<sup>2-</sup> (latt) in  $\alpha$ -MnO<sub>2</sub> surface is considered to be the primary active species for activating the C–H bond.

### 3.5. In situ DRIFTS

In situ DRIFTS experiments were performed to determine the intermediate species presented in the catalytic oxidation of methane over  $\alpha$ -MnO<sub>2</sub>. In the case of a flow of 1% CH<sub>4</sub> + N<sub>2</sub> (Fig. 10A), the band at 3016 cm<sup>-1</sup> is related to C–H stretching vibrations of CH<sub>n</sub> species [20]. The band at 1613 cm<sup>-1</sup> is associated with asymmetric and symmetric vibrations of –O–CH(=O) species. Moreover, the bands at 1539 and 1304 cm<sup>-1</sup> are ascribed to  $\nu_a$ (COO) and  $\nu_s$ (COO) stretching on Mn<sup>4+</sup> sites, while the peak at 1149 cm<sup>-1</sup> is related to C–O vibrational frequency of surface COO–[21]. Regarding the weak absorption bands at 2343 and 2894 cm<sup>-1</sup>, they are attributed to gaseous CO<sub>2</sub> and C–H stretching vibration of the surface –OCH<sub>3</sub> species, respectively.

In the presence of 20%O<sub>2</sub> at 250 °C (Fig. 10B), new band at 3602 cm<sup>-1</sup> associated with  $\alpha$ -MnO<sub>2</sub> surface hydroxyl groups appears. Further heating up to 350 °C (Fig. 10C), the 2894 cm<sup>-1</sup> band intensity decreases, giving rise to an additional band at 2993 cm<sup>-1</sup> associated with the surface formate species. These results confirm the oxidation of the adsorbed –CH<sub>3</sub>O species to the formate species. After the introduction of O<sub>2</sub> flow at 450 °C for 20 min (Fig. 10D), the above bands almost disappear, indicating that intermediate species are completely oxidized to CO<sub>2</sub> and H<sub>2</sub>O.

When 9.5vol%H<sub>2</sub>O (Fig. 10E) was introduced into the system, CH<sub>n</sub>, CH<sub>n</sub>–O–CH(=O) and –COO stretching vibration bands are greatly decreased in intensity, while the –OH stretching vibration band at 3484 cm<sup>-1</sup> is increased in intensity, indicating the competitive adsorption of H<sub>2</sub>O and CH<sub>4</sub> on MnO<sub>2</sub>, resulting in the decrement of

catalytic activity in the presence of 9.5 vol% H<sub>2</sub>O at relatively low temperature. When  $\alpha$ -MnO<sub>2</sub> was exposed to 1 vol% CH<sub>4</sub> + 10 vol% CO<sub>2</sub> and balanced by N<sub>2</sub> at 200 °C, a strong band appears around 998 cm<sup>-1</sup>, suggesting the formation of the carbonate species [20]. These carbonate species may cover surface Mn<sup>4+</sup> active sites, resulting in a quick decrement of methane conversion.

### 3.6. Transition-state analysis and reaction mechanism

#### 3.6.1. Transition-state studies

According to HR-TEM results,  $\alpha$ -MnO<sub>2</sub> and  $\beta$ -MnO<sub>2</sub> mainly contain (100) and (101) exposed planes, respectively, thus, DFT calculation was carried out to further identify the reaction sites and the C–H dissociation modes in  $\alpha$ -MnO<sub>2</sub>(100) and  $\beta$ -MnO<sub>2</sub>(101). The calculated energy profiles of  $\alpha$ -MnO<sub>2</sub> (100) and  $\beta$ -MnO<sub>2</sub> (101) surface are displayed in Fig. 11. The optimized structures of intermediates pathway in CH<sub>4</sub> oxidation over  $\alpha$ -MnO<sub>2</sub> (100) and  $\beta$ -MnO<sub>2</sub> (101) surfaces are shown in Fig. 12. Additionally, the top and side views of clean  $\alpha$ -MnO<sub>2</sub> (100) and  $\beta$ -MnO<sub>2</sub> (101) surfaces are provided in Fig. S8, and more configurations involved in the minimum energy path (MEP) of methane oxidation are provided in the Supporting Information (see Fig. S9).

Firstly, CH<sub>4</sub> adsorbs on the surface of  $\alpha$ -MnO<sub>2</sub> (100) (Fig. 11A) and  $\beta$ -MnO<sub>2</sub> (101) (Fig. 11B) via physical adsorption, and their adsorption energies are close to each other calculated by DFT + U (adsorption energy is defined as a net difference between the total energy of the adsorption system and those of each pristine state). Then, an surface bridged oxygen atoms (O\*) together with a Mn site, forms a metal–oxygen site-pair (\*–O\*–Mn) that assists with the kinetically relevant H abstraction from CH<sub>4</sub>, forming an adsorbed CH<sub>3</sub>\* and H\* species on both  $\alpha$ -MnO<sub>2</sub> (100) and  $\beta$ -MnO<sub>2</sub>(101). The formed CH<sub>3</sub>\* intermediate species have been proved by *in situ* DRIFTS and CH<sub>4</sub>-TPR-MS results. Meanwhile, the formed CH<sub>3</sub>\* continues to adsorb on the surface bridged oxygen atoms only on  $\beta$ -MnO<sub>2</sub> surface. Secondly, a dissociation process of CH<sub>3</sub>\* to CH<sub>2</sub>\* takes place on both  $\alpha$ -MnO<sub>2</sub> and  $\beta$ -MnO<sub>2</sub>, which is similar to that of CH<sub>4</sub> to CH<sub>3</sub>\*. Briefly, the H atom abstracted from CH<sub>3</sub>\* transfers to bridged oxygen atom, resulting in the generation of H<sub>2</sub>O (g) and O-vacancy on these Mn oxides surface. O<sub>2</sub> gas molecule is adsorbed on the surface bridging oxygen defect site, which is attributed to H<sub>2</sub>O being removed from the surface of  $\alpha$ -MnO<sub>2</sub> (100). To be noted, the energy barrier of CH<sub>3</sub>\* to CH<sub>2</sub>\* in  $\alpha$ -MnO<sub>2</sub> (E<sub>b</sub> = 0.54 eV) is lower than that in  $\beta$ -MnO<sub>2</sub> (E<sub>b</sub> = 0.96 eV), suggesting the transformation of CH<sub>3</sub>\* to CH<sub>2</sub>\* species is easier in the former catalyst.

Thirdly, the intermediate CH<sub>2</sub>\* transforms to CH\* by means of CH<sub>2</sub>\* dehydrogenation on surface O-vacancy (Fig. 12). Furthermore, the DFT + U calculation results suggest that the pathway from CH\* to H\* is more difficult than that of CH<sub>2</sub>\* dehydrogenation over both  $\alpha$ -MnO<sub>2</sub> and  $\beta$ -MnO<sub>2</sub>. Removal of the fourth H atom needs to overcome the energy barrier of 0.84 eV in  $\alpha$ -MnO<sub>2</sub>, lower than that in  $\beta$ -MnO<sub>2</sub> (E<sub>b</sub> = 0.97 eV). Thus, the transformation of CH\* to H\* species occur more easily for  $\alpha$ -MnO<sub>2</sub>. Note that surface active oxygen plays an important role in the CH\* dehydrogenation process. Specifically, H atom in CH\* transfers to surface active oxygen atoms of Mn oxides, giving rise to the formation of CO<sub>2</sub>. Meanwhile, the reduced surface oxygen defects are regenerated immediately through the desorption of gaseous CO<sub>2</sub>. The energy profiles of CH<sub>4</sub> oxidation indicate that the oxidation of methane over  $\alpha$ -MnO<sub>2</sub> is easier with respect to  $\beta$ -MnO<sub>2</sub>. The rate-determining step in  $\alpha$ -MnO<sub>2</sub> is the removal of the last H atom, while that in  $\beta$ -MnO<sub>2</sub> is the dehydrogenation of CH<sub>3</sub>\* to CH<sub>2</sub>\* and CH\* to H\*.

#### 3.6.2. Regeneration of surface active sites

Despite hydrogen transfer between surface bridged oxygen probably temporarily recover the reactivity of oxygen species close to the reaction intermediate, the continuously accumulated H atoms will block these sites eventually once they cannot leave the surface. Therefore, the desorption of hydrogen-containing species for the removal of these hydrogen atoms are important to the catalytic cycle. According to the *in*

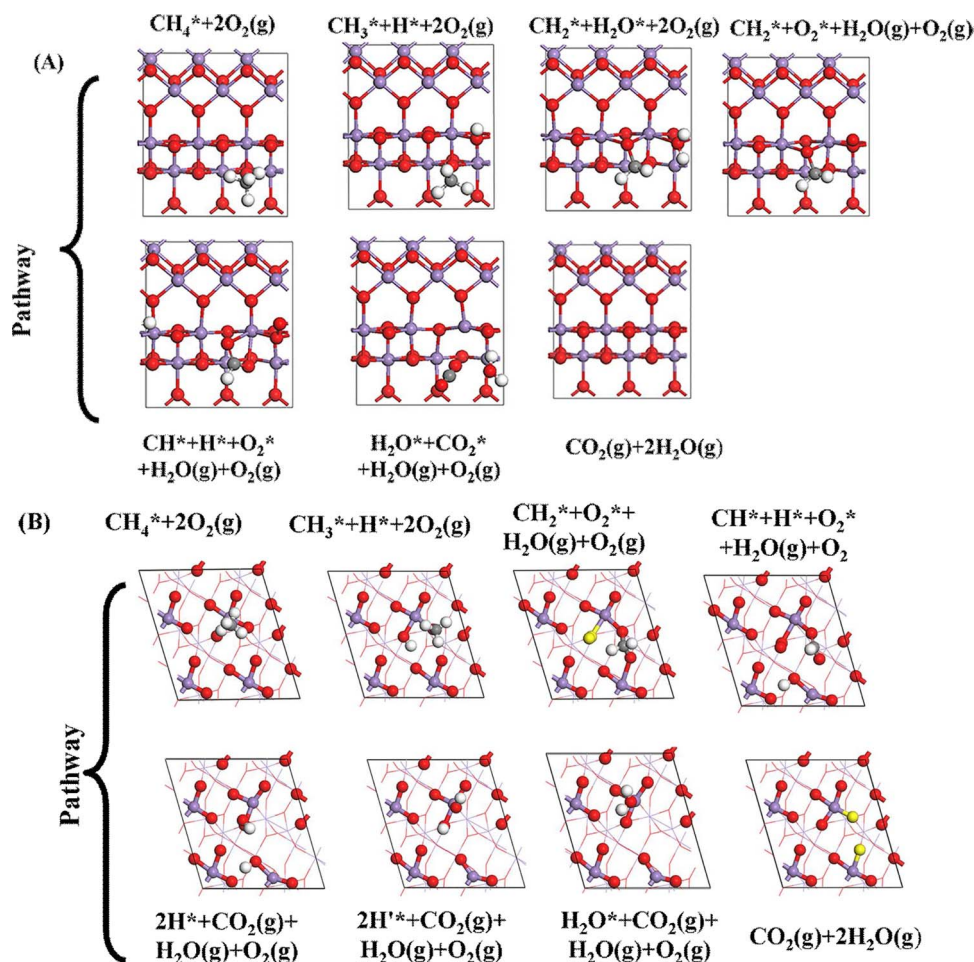


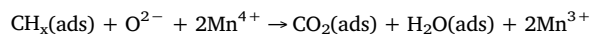
Fig. 12. The optimized structures of intermediates pathway in CH<sub>4</sub> oxidation over (A) α-MnO<sub>2</sub> (100) and (B) β-MnO<sub>2</sub> (101).

*in situ* DRIFTS results, carboxylates are the primary intermediate species, and these possible –COOH and –CH<sub>3</sub>O species containing H can be converted into H<sub>2</sub>O and CO<sub>2</sub> in the presence of oxygen atmosphere at a relatively high temperature. Furthermore, the barrier of the H<sup>+</sup> unites with the O atom can be easily conquered, converting to CO<sub>2</sub> and H<sub>2</sub>O at relatively high temperature. Finally, complete faces of α-MnO<sub>2</sub> and β-MnO<sub>2</sub> are regenerated by mean of gaseous O<sub>2</sub> adsorbing on the surface defects (Fig. 12).

### 3.6.3. Reaction mechanism

Based on *in situ* DRIFTS and TSS results, CH<sub>4</sub> dissociates on Mn<sup>4+</sup> sites to generate CH<sub>3</sub><sup>\*</sup>, CH<sub>2</sub><sup>\*</sup> and CH<sup>\*</sup>. Subsequently, CH<sup>\*</sup> interacts with surface active oxygen species to form H<sup>+</sup> and CO<sub>2</sub>. On the other hand, methane is activated on the reduced Mn sites to form CH<sub>n</sub><sup>\*</sup> and H<sup>\*</sup>. During these processes, a hydrogen atom leaves the cracked CH<sub>4</sub> and stays as H<sup>+</sup> on the surface and probably links to an oxide ion, giving rise to –OH. Additionally, H<sup>+</sup> is able to readily shift among various surface oxygen species to generate adsorbed H<sub>2</sub>O\* for the rapid regeneration of surface active oxygen species. Then, active oxygen species react with CH<sub>3</sub><sup>\*</sup> to form the –COO and –CH<sub>3</sub>O species, and the whole process involves the interaction of σ and σ\* C–H orbitals with 3d electrons. EXAFS results indicate that a higher fraction of longer Mn–O–Mn bridges is existed in α-MnO<sub>2</sub>, that is a more disordered structure in the octahedra ligand field of the fixed oxo bridges. The surface oxo sites where gases (CH<sub>4</sub> or O<sub>2</sub>) can bind are expected to be relatively labile for the antibonding electron. This could be a key contributor to the release of surface oxygen species [16]. O<sub>2</sub>-TPD-MS studies indicate that α-MnO<sub>2</sub> possesses more active oxygen species and easier release of O<sup>2–</sup> species than Meso-MnO<sub>2</sub>, β-MnO<sub>2</sub> and α-Mn<sub>2</sub>O<sub>3</sub>.

These oxygen species are considered to be the primary active species for activating the C–H bond, as illustrated by the following equation:



Moreover, CH<sub>4</sub>-TPR-MS results also suggest that α-MnO<sub>2</sub> displays lower activation temperature for dissociating CH<sub>4</sub> to CH<sub>n</sub><sup>\*</sup> and H<sup>\*</sup> compared to other catalysts. After adding 20%O<sub>2</sub>, the –COO and –CH<sub>3</sub>O intermediate species can be oxidized to CO<sub>2</sub> and H<sub>2</sub>O. Additionally, the TSS study results show that the dehydrogenation of CH<sup>\*</sup> to H<sup>+</sup> (E<sub>b</sub> = 0.84 eV) products is the rate-determining step in α-MnO<sub>2</sub>. Combined with the above analysis, methane combustion over MnO<sub>2</sub> catalyst also proceeds via both the routes of MvK and L-H mechanisms while the latter is also predominant.

## 4. Conclusions

To summarize, the roles of crystallographic structure in methane oxidation over Mn oxides were studied. The results demonstrate that catalytic activity follows an order of α-MnO<sub>2</sub> > β-MnO<sub>2</sub> > α-Mn<sub>2</sub>O<sub>3</sub> > Meso-MnO<sub>2</sub>. Meanwhile, α-MnO<sub>2</sub> exhibits excellent 9.5 vol% H<sub>2</sub>O and/or 10 vol%CO<sub>2</sub> resistance ability. The superior catalytic performances in α-MnO<sub>2</sub> could be attributed to several factors, including the existence of more mono-μ-oxo bridged (corner-shared) MnO<sub>6</sub> sites, higher surface Mn concentration and active oxygen species, and better reducibility. Moreover, *in situ* DRIFTS studies demonstrate that –COO and –CH<sub>3</sub>O are the key intermediate species, which are oxidized by active oxygen species to CO<sub>2</sub> and H<sub>2</sub>O. TSS studies in CH<sub>4</sub> combustion over α-MnO<sub>2</sub> indicate that the dehydrogenation of CH<sup>\*</sup> to H<sup>+</sup> is the rate-determining step. Besides, the combustions of methane over MnO<sub>2</sub>

involve both the MvK and L-H mechanisms, and the latter is more dominant. Our study demonstrates that the structure-related catalytic activities could provide guidance in the further development of easily prepared, scalable, and low-cost catalysts for methane combustion based on TMOs and their derivatives.

## Acknowledgments

This work was financially supported by National key research and development program (2016YFC0203902), the National Natural Science Foundation of China (21703037, 21407025, 21773030), and leading project of Fujian Province (2017H0049).

## Appendix A. Supplementary data

Supplementary material related to this article can be found, in the online version, at doi:<https://doi.org/10.1016/j.apcatb.2018.02.007>.

## References

- [1] (a) G. Ercolino, P. Stelmachowski, G. Grzybek, A. Kotarba, S. Specchia, *Appl. Catal. B Environ.* 206 (2017) 712–725;  
(b) A. Gremminger, P. Lott, M. Merts, M. Casapu, J.-D. Grunwaldt, O. Deutschmann, *Appl. Catal. B Environ.* 218 (2017) 833–843;  
(c) J. Chen, X. Zhang, H. Arandiyán, Y. Peng, H. Chang, J. Li, *Catal. Today* 201 (2013) 12–18;  
(d) Z. Rui, Y. Huang, Y. Zheng, H. Ji, X. Yu, *J. Mol. Catal. A Chem.* 372 (2013) 128–136.
- [2] (a) X. Zou, Z. Rui, H. Ji, *ACS Catal.* 7 (2017) 1615–1625;  
(b) J.J. Willis, E.D. Goodman, L. Wu, A.R. Riscoe, P. Martins, C.J. Tassone, M. Cargnello, *J. Am. Chem. Soc.* 139 (2017) 11989–11997;  
(c) S. Xie, Y. Liu, J. Deng, X. Zhao, J. Yang, K. Zhang, Z. Han, H. Arandiyán, H. Dai, *Appl. Catal. B Environ.* 206 (2017) 221–232;  
(d) I.E. Beck, V.I. Bukhtiyarov, I.Y. Pakharukov, V.I. Zaikovskiy, V.V. Kriventsov, Parmon, V. N. *J. Catal.* 268 (2009) 60–67.
- [3] F.F. Tao, J. Shan, L. Nguyen, *Nat. Commun.* 6 (2015) 7798.
- [4] L.F. Liotta, H. Wu, G. Pantaleo, A.M. Venezia, *Catal. Sci. Technol.* 3 (2013) 3085–3102.
- [5] F. Wang, H. Dai, J. Deng, G. Bai, K. Ji, Y. Liu, *Environ. Sci. Technol.* 46 (2012) 4034–4041.
- [6] Y. Meng, W. Song, H. Huang, Z. Ren, S. Chen, S.L. Suib, *J. Am. Chem. Soc.* 136 (2014) 11452–11464.
- [7] L.F. Liotta, H. Wu, G. Pantaleo, A.M. Venezia, *Catal. Sci. Technol.* 3 (2013) 3085–3102.
- [8] W. Hu, J. Lan, Y. Guo, X.-M. Cao, P. Hu, *ACS Catal.* 5 (2016) 5508–5519.
- [9] F. Zasada, W. Piskorz, Z. Sojka, *J. Phys. Chem. C* 119 (2015) 19180–19191.
- [10] F. Zasada, W. Piskorz, J. Janas, J. Grybos, P. Indyka, Z. Sojka, *ACS Catal.* 5 (2015) 6879–6892.
- [11] D.M. Robinson, Y.B. Go, M. Mui, G. Gardner, Z. Zhang, D. Mastrogianni, E. Garfunkel, J. Li, M. Greenblatt, G.C. Dismukes, *J. Am. Chem. Soc.* 135 (2013) 3494–3501.
- [12] (a) Y. Liu, H. Dai, J. Deng, S. Xie, H. Yang, W. Tan, W. Han, Y. Jiang, G. Guo, *J. Catal.* 309 (2014) 408–418;  
(b) L.C. Wang, X.S. Huang, Q. Liu, Y.M. Liu, Y. Cao, H.Y. He, K.N. Fan, J.H. Zhuang, *J. Catal.* 259 (2008) 66–74.
- [13] (a) S.H. Lee, T.W. Kim, D.H. Park, J.-H. Choy, S.-J. Hwang, N. Jiang, S.-E. Park, Y.-H. Lee, *Chem. Mater.* 19 (2007) 5010–5017;  
(b) A. Longo, L.F. Liotta, G.D. Carlo, F. Giannici, A.M. Venezia, A. Martorana, *Chem. Mater.* 22 (2010) 3952–3960.
- [14] Y. Luo, Y.-Q. Deng, W. Mao, X.-J. Yang, K. Zhu, J. Xu, Y.-F. Han, *J. Phys. Chem. C* 116 (2012) 20975–20981.
- [15] A.G.M. Silva, C.M. Kisukuri, T.S. Rodrigues, E.G. Candido, I.C. Freitas, A.H.M. Silva, J.M. Assaf, D.C. Oliveira, L.H. Andrade, P.H.C. Camargo, *Appl. Catal. B Environ.* 184 (2016) 35–43.
- [16] I. Zaharieva, P. Chernev, M. Risch, K. Klingan, M. Kohlhoff, A. Fischer, H. Dau, *Energy Environ. Sci.* 5 (2012) 7081–7089.
- [17] W. Si, Y. Wang, Y. Peng, J. Li, *Angew. Chem. Int. Ed.* 54 (2015) 7954–7957.
- [18] S. Chen, L. Zeng, H. Tian, X. Li, J. Gong, *ACS Catal.* 7 (2017) 3548–3559.
- [19] Y. Lou, J. Ma, W. Hu, Q. Dai, L. Wang, W. Zhan, Y. Guo, X.-M. Cao, Y. Guo, P. Hu, G. Lu, *ACS Catal.* 6 (2016) 8127–8139.
- [20] X. Zou, Z. Rui, S. Song, H. Ji, *J. Catal.* 338 (2016) 192–201.
- [21] P.J. Jodłowski, R.J. Jędrzejczyk, D. Chlebda, M. Gierada, J. Łojewska, *J. Catal.* 350 (2017) 1–12.